

17. Ebert A, Herzog H, Stöcklin G, et al. Kinetics of 14(R,S)-fluoro-18-fluoro-6-thiaheptadecanoic acid in normal human hearts at rest, during exercise and after dipyrindamole injection. *J Nucl Med* 1994;35:51-56.
18. Althoefer C, vom Dahl J, Bares R, Stocklin GL, Bull U. Metabolic mismatch of septal beta-oxidation and glucose utilization in left bundle branch bloc assessed with PET. *J Nucl Med* 1995;36:2056-2059.
19. Schultz G, vom Dahl J, Kaiser H, et al. Imaging of  $\beta$ -oxidation by static PET with 14(R,S)-[<sup>18</sup>F]-fluoro-6-thiaheptadecanoic acid (FTHA) in patients with advanced coronary heart disease: a comparison with <sup>18</sup>FDG PET and <sup>99m</sup>Tc-MIBI SPET. *Nucl Med Commun* 1996;17:1057-1064.
20. Knuuti MJ, Nuutila P, Ruotsalainen U, et al. Euglycemic hyperinsulinemic clamp and oral glucose load in stimulating myocardial glucose utilization during positron emission tomography. *J Nucl Med* 1992;33:1255-1262.
21. DeFronzo R, Tobin J, Andres R. Glucose clamp technique: a method for quantifying insulin secretion and resistance. *Am J Physiol* 1979;237:E214-E223.
22. Clark J, Crouzel C, Meyer G, Strijkmans K. Current methodology for oxygen-15 production for clinical use. *Appl Radiat Isot* 1987;38:597-600.
23. Crouzel C, Clark J, Brihaye C, et al. Radiochemistry automation for PET. In: Stöcklin G, Pike V, eds. *Radiopharmaceuticals for positron emission tomography*. Dordrecht, The Netherlands: Kluwer Academic Publishers; 1993:45-90.
24. DeGrado T. Synthesis of 14(R,S)-[<sup>18</sup>F]-fluoro-6-thiaheptadecanoic acid (FTHA). *J Lab Compd Radiopharm* 1991;24:889-995.
25. Mäki M, Luotolahti M, Nuutila P, et al. Glucose uptake in the chronically dysfunctional but viable myocardium. *Circulation* 1996;93:1658-1666.
26. Raitakari M, Knuuti J, Ruotsalainen U, et al. Insulin increases blood volume in human skeletal muscle: studies using [<sup>15</sup>O]CO and positron emission tomography. *Am J Physiol* 1995;269:E1000-E1005.
27. Patlak CS, Blasberg RG. Graphical evaluation of blood-to-brain transfer constants from multipletime uptake data. Generalizations. *J Cereb Blood Flow Metab* 1985;5:584-590.
28. Schiller N, Shah P, Crawford M, et al. Recommendations for quantitation of the left ventricle by two-dimensional echocardiography. *J Am Soc Echocardiogr* 1989;2:358-367.
29. Kadish A, Little R, Sternberg J. A new and rapid method for the determination of glucose by measurement of rate of oxygen consumption. *Clin Chem* 1968;14:116-131.
30. Marbach E, Weil M. Rapid enzymatic measurement of blood lactate and pyruvate. *Clin Chem* 1967;13:314-325.
31. Fox K, Abendschein D, Ambos H, Sobel B, Bergmann S. Efflux of metabolized and nonmetabolized fatty acid from canine myocardium. Implications for quantifying myocardial metabolism tomographically. *Circ Res* 1985;57:232-243.
32. van der Vusse G, Roemen Th, Prinzen F, Coumans W, Reneman R. Uptake and tissue content of fatty acids in dog myocardium under normoxic and ischemic conditions. *Circ Res* 1982;50:538-546.
33. Wisneski J, Gertz E, Neese R, Mayr M. Myocardial metabolism of free fatty acids. Studies with <sup>14</sup>C-labeled substrates in humans. *J Clin Invest* 1987;79:359-366.
34. Nellis S, Liedtke A, Renstrom B. Fatty acid kinetics in aerobic myocardium: characteristics of tracer carbon entry and washout and influence of myocardial demand. *J Nucl Med* 1992;33:1864-1874.

# Quantitation of Presynaptic Cardiac Sympathetic Function with Carbon-11-Meta-Hydroxyephedrine

James H. Caldwell, Keith Kroll, Zheng Li, Katherine Seymour, Jeanne M. Link and Kenneth A. Krohn  
 Division of Cardiology and Departments of Bioengineering and Radiology, Veterans Administration Medical Center, and the University of Washington, Seattle, Washington

The purpose of this study was to validate an axially distributed blood-tissue exchange model for the quantitation of cardiac presynaptic sympathetic nervous system function that could be applied to PET images. The model accounts for heterogeneity in myocardial blood flow, differences in transport rates of <sup>11</sup>C-meta-hydroxyephedrine (mHED) across the capillary endothelium and/or neuronal membranes, the virtual volumes of distribution in the interstitial space and neuron and retention of mHED in the neuronal vesicles. **Methods:** Multiple indicator outflow dilution and residue detection methods were used to measure the kinetics of radiolabeled intravascular space and interstitial space markers and <sup>11</sup>C-mHED in isolated perfused rat heart at baseline and during norepinephrine neuronal transporter blockade with desipramine (DMI). The outflow dilution and residue detection data were modeled with a multiple pathway, four-region, axially distributed model of blood-tissue exchange describing flow in the capillary and exchange between regions using permeability-surface area products with units of clearance of milliliters per minute per gram. Meta-hydroxyephedrine may enter the nerve terminal via membrane transport, where it may be sequestered by first-order unidirectional uptake within vesicles. Release of mHED from the vesicles is modeled via exchange with the interstitial space. **Results:** After intracoronary injection, mHED transport across the capillary endothelium and in the interstitial space closely followed that of sucrose. Subsequently, mHED was retained in the heart, whereas sucrose washed out rapidly. With DMI the outflow dilution curves more closely resembled those of sucrose. Model parameters reflecting capillary-interstitial kinetics and volumes of distribution were unchanged by DMI, whereas parameters reflecting the neuronal transporter process and volumes of distribution in the nerve terminal and vesicular sequestration were markedly decreased by DMI. Application of the model to a pilot set of canine PET images of mHED

suggests the feasibility of this approach. **Conclusion:** Meta-hydroxyephedrine kinetics in the heart can be quantitated using an axially distributed, blood-tissue exchange model that accounts for heterogeneity of flow, reflects changes in neuronal function and is applicable to PET images.

**Key Words:** sympathetic nervous system; PET; modeling; meta-hydroxyephedrine; neuronal transporter

*J Nucl Med* 1998; 39:1327-1334

Substantial and increasing evidence supports the concept that aberrations in cardiac sympathetic nervous system (SNS) function contribute to and may be primarily responsible for the morbidity and mortality associated with cardiac conditions such as sudden cardiac death (1), congestive heart failure (2-4) and post-myocardial infarction depression (5,6). A major limitation to understanding the role of the SNS in these conditions has been the absence of quantitative methods for noninvasive examination of global and/or regional pre- and postsynaptic cardiac SNS function.

The distribution and retention in the myocardium of norepinephrine (NE) analogs (7-9) and the postsynaptic  $\beta$ -adrenergic receptor density and distribution (10) can now be imaged using PET. Several positron-emitting compounds have been developed to study presynaptic SNS function (11-14). Among these, <sup>11</sup>C-meta-hydroxyephedrine (mHED), a tracer for the norepinephrine transporter (NET) mechanism (15) that recycles NE released from the sympathetic nerve terminal, has been shown to have clinical applicability (7-9). Carbon-11-labeled mHED has a high affinity for the NET sites. NET and vesicular storage are similar to that of NE, and <sup>11</sup>C-mHED has the advantage of limited metabolism of the tracer (16,17). It has low nonspecific

Received Mar. 11, 1997; revision accepted Oct. 21, 1997.

For correspondence or reprints contact: James H. Caldwell, MD, Division of Cardiology (111C), Veterans Administration Medical Center, Seattle, WA 98108.

binding and can be labeled with sufficiently high specific activity to avoid measurable physiologic effects (18,19).

Several PET imaging studies in humans have demonstrated that a semiquantitative analysis method was capable of detecting large differences in the regional retention of mHED (7–9). However, there has been little attempt to account for physiological variables such as:

1. differences in the delivery of the radiotracer, including diffusion gradients along the capillary length, and the effects of flow heterogeneity;
2. differences in transport into the neuroeffector junction;
3. potential retention of local or systemic metabolites; or
4. distribution into various compartments within the neuroeffector region.

Accounting for such variables might improve our understanding of disease processes as well as improve the sensitivity or specificity for differentiating disease states.

Preliminary attempts at quantitation of mHED images have been reported by Hutchins et al. (20), in which a three-compartment model showed, in canine studies, a strong correlation ( $r = 0.875$ ) between modeled regional NE tissue distribution volumes and measured tissue NE concentrations. The model parameter representing cellular and vesicular NET,  $k_3$ , was reduced (45–60%) in the presence of the NET blocker desipramine (DMI). Application of this model to human images has not been reported.

DeGrado et al. (17) have expanded our understanding of the transport capacities and volumes of distribution ( $V_d$ ) of  $^{11}\text{C}$ -mHED through washout residue detection studies in isolated perfused rat hearts. However, methodological constraints allowed them to calculate only global washin and washout rates and a single  $V_d$ . Perturbations of the system with the NET blocker DMI decreased uptake and produced rapid clearance. Norepinephrine increased the clearance rate and decreased  $V_d$ . Based on their results and existing knowledge of NE kinetics, they proposed a model for mHED but did not test it.

To better quantify presynaptic neuronal function in the intact heart, we have developed an axially distributed blood–tissue exchange model that accounts for heterogeneity in myocardial blood flow, the transport rates of mHED across the capillary endothelium and neuronal membranes, the virtual volumes of distribution in the interstitial space and neuron, the retention of mHED in the neuronal vesicles and the release of mHED via exocytosis. We report here our validation of this model in isolated perfused hearts and a single feasibility study of model application to PET images.

## MATERIALS AND METHODS

### Experimental Preparation: Rat

Male Sprague-Dawley rats, 200–300 g, were heparinized (1000 units) and anesthetized with pentobarbital sodium (150 mg/kg) intraperitoneally. The chest was opened by making bilateral incisions from the costal margins to the clavicles, and the wall was folded upward. To prevent ischemia, the aorta was rapidly cannulated, and retrograde perfusion was started with an oxygenated (37°C) modified Krebs-Henseleit buffer solution containing 123 mM NaCl, 4.8 mM KCl, 1.2 mM  $\text{NaHCO}_3$ , 6.7 mM glucose, 2 mM  $\text{CaCl}_2$ , 1.2 mM  $\text{KH}_2\text{PO}_4$ , 2 mM pyruvate, 10 mg/liter EDTA and 20 mg/liter ascorbic acid (Sigma Chemical Co., St. Louis, MO). The pulmonary artery was incised to allow outflow of the perfusate, the flow of which was controlled by a calibrated roller pump (Gilson Co., Middleton, WI). After ligation of the vena cavae, the heart was removed from the thorax and hung from a stainless steel cannula mounted on a flexible support arm. To collect coronary sinus

drainage, the pulmonary artery was isolated and cannulated with a 8-cm piece of perforated polyethylene tubing (1.4-mm inside diameter), its distal end was advanced through the right ventricular free wall and the tubing was connected to an in-house fabricated computer-controlled collection device. A latex balloon was inserted in the left ventricle through the left atrium and mitral valve and connected to a pressure transducer (Gould, Inc., Oxnard, CA) to monitor left ventricular pressure and heart rate and to maintain left ventricular (LV) end diastolic pressure in a physiologic range (0–5 mmHg).

For some of the experiments, residue detection of the whole heart was performed with two 3-inch NaI(Tl) detectors (Bicron, Newbury, OH) used in coincidence mode and positioned to give maximal recovery of the annihilation events occurring in the heart (Canberra Co., Meriden, CT). Analog and digital data were collected on-line using ASYST (Keithley Asyst, Inc., Rochester, NY), a personal computer-based program. Sampling rates were 1 Hz for the tracer  $^{11}\text{C}$ .

### Experimental Protocol

Heart rate and LV systolic and diastolic pressure were recorded continuously, and values were measured immediately before each of the multiple indicator dilution (MID) runs. Timed coronary sinus flow and leakage flow (fluid dripping from the epicardial surface of the heart) were collected in separate graduated cylinders at the time of the hemodynamic measurements. Injectate solutions were made by combining aliquots of stock solutions of  $^{125}\text{I}$ -bovine serum albumin ( $^{125}\text{I}$ -BSA; ICN Biomedical, Irvine, CA) as the marker for the intravascular space,  $^3\text{H}$ -sucrose (American Radiolabeled Chemicals, St. Louis, MO) to measure the interstitial space (isf), and  $^{11}\text{C}$ -mHED as the test substance. Tritiated sucrose was used as the reference isf marker because it has a molecular weight similar to that of mHED. Carbon-11-labeled meta-hydroxyephedrine was made according to the method of Rosenspire et al. (18). The  $^{11}\text{C}$ -mHED product was purified by semipreparative high-performance liquid chromatography using an Inertsil ODS-2  $\text{C}_{18}$  column (Metachem, Torrance, CA; 10 mm  $\times$  250 mm, 5- $\mu\text{m}$  particles) eluted with 0.15 M sodium acetate (pH 6) and ethanol (95:5, v/v) (19). The retention volume for mHED was 55 ml. Chemical purity was assayed using an Inertsil ODS-2  $\text{C}_{18}$  column (4.6 mm  $\times$  250 mm) eluted with 0.2 M ammonium formate (pH 6) and acetonitrile (95:5, v:v) and ultraviolet absorbance detection at 272 nm. Retention was verified against standards of metamamol and mHED. Retention volumes for metamamol and mHED were 7.4 and 10.7 ml, respectively. The  $^{11}\text{C}$ -mHED was >98% pure, with a measured specific activity >2000 Ci/mmol at the end of production of the radionuclide.

Injectate (~100  $\mu\text{l}$ ) containing 3–5  $\mu\text{Ci}$  of  $^{125}\text{I}$ -BSA, 2–5  $\mu\text{Ci}$  of  $^3\text{H}$ -sucrose and 10–50  $\mu\text{Ci}$  of  $^{11}\text{C}$ -mHED was drawn into a hubless plastic syringe with an integrated 26-gauge needle. The syringe was weighed after the injectate was drawn into it and again after injection. The needle of the injectate syringe was passed through a piece of SILASTIC tubing (Dow Corning, Midland, MI) just proximal to the cannula, and the radiotracers were injected as a bolus (~100  $\mu\text{l}$ ) into the perfusate line. A 1-ml volume of tubing plus cannula was present between the injection site and the heart. Beginning with tracer injection, the total effluent from the coronary sinus was collected directly into preweighed counting tubes in the fraction collector. Samples were collected every second for 20 sec, every 2 sec for 10 sec, every 5 sec for the next 30 sec and every 10 sec during the next 60 sec (total collection period = 2 min). Studies were performed under basal conditions ( $n = 5$ ) or during perfusion with Krebs-Henseleit buffer (as above) containing desipramine (20  $\mu\text{M}$ ), which was started 10–15 min before radiotracer injection.

Residue detection data were collected for 30 min after radiotracer injection.

### Data Preparation

The effluent tubes along with standards taken from the injectate pool were counted for  $^{11}\text{C}$  in a Packard Cobra multiple detector counter (Packard Instruments, Meriden, CT) with a 20% energy window centered about the 511-keV gamma peak. Carbon-11 activity was decay corrected and expressed as counts per minute per milliliter. After completion of the  $^{11}\text{C}$  counting, the tubes were weighed and counted for  $^3\text{H}$  and  $^{125}\text{I}$  in a Packard Tricarb liquid scintillation counter, corrected for decay and crosstalk between  $^3\text{H}$  and  $^{125}\text{I}$  and expressed as counts per minute per milliliter (21). All effluent count data were then expressed as the fraction ( $h_i$ ) of the injected dose appearing in the outflow sample at that sample time.

Dilution curves for albumin, sucrose and mHED were normalized to injected activity using the expression,  $h(t) = F \times C(t)/q_0$ , where  $h(t)$  is the fraction of injected tracer emerging in the coronary outflow per second,  $F$  is the coronary flow rate (milliliters per second),  $C(t)$  is the tracer activity in the samples of venous effluent perfusate (counts per minute per milliliter) and  $q_0$  is the activity (counts per minute) injected in the bolus. Residue detection activity was corrected for background and radioactivity decay, and the data were transferred to a UNIX-based workstation for model analysis (Sun Microsystems, Palo Alto, CA).

### Modeling

Data from the multiple indicator dilution and the PET experiments were analyzed using a mathematical model that describes the processes governing the distribution and kinetics of bloodborne tracers in the heart. The use of the model followed general principles developed by Bassingthwaite and Goresky (22) and Kuikka and coworkers (23). The model accounts for the effects of regional flow heterogeneity by using multiple flow pathways arranged in parallel. Each of the pathways consisted of an exchange unit (Fig. 1) describing capillary, interstitial, nerve terminal and vesicle regions. Delay and dispersion of the tracers in nonexchanging coronary arterioles and venules were described using a vascular operator (volume = 0.08 ml/g, relative dispersion = 0.48) (24) in series with the exchange unit in each of the model flow pathways. In each pathway, the model describes flow ( $F_p$ ) in the capillary ( $V_p$ ) and radial exchange between regions using permeability-surface area (PS) products with units of clearance of milliliters per minutes per gram. To account for the broad range of diffusion distances between sites in the isf that are close to and far from the capillary membrane, mathematically the isf is considered as having two equal volumes,  $V_{isf1}$  and  $V_{isf2}$ , with diffusional exchange between the two parts ( $PS_{isf}$ ).

After entering the isf from the capillary ( $PS_g$ ), mHED may enter the nerve terminal ( $V'_{nt}$ ) via membrane transport ( $PS_{nt}$ ), where it may be sequestered ( $G_{seq}$ ) by first-order unidirectional uptake within vesicles ( $V'_{ves}$ ). Although not physiologically exact, release of mHED from the vesicles is modeled via exchange with the isf ( $PS_{ves}$ ). It is assumed that there is neither irreversible binding nor metabolism of mHED. The use of a PS function to model the vesicular exocytosis of mHED was an operational necessity imposed by the structure of the model.

The parallel exchange pathways share a common inlet by which tracers enter the system and a common outlet by which tracers exit. Only one of these exchange pathways is shown in Figure 1. The common inlet includes two nonexchanging vascular operators arranged in series to describe tracer delay and dispersion in large epicardial coronary vessels ( $V = 0.15$  ml/g,  $RD = 0.24$ ) and in tubing of the perfusion apparatus and the sample collecting system ( $V = 0.1$  ml/g,  $RD = 0.24$ ) (24). The model solution for the

residue function included the total tracer quantity in all regions of the exchange unit and in all the nonexchanging elements.

### Multiple Tracer Studies in Rat Hearts

To minimize the number of degrees of freedom during parameter optimization, certain model parameters were given preassigned values based on experimental measurements (flow) or a priori knowledge. The capillary volume ( $V_p$ ) was assigned a value of 0.035 ml/g based on anatomic considerations (25), and the volumes and relative dispersions of the nonexchanging elements were held constant at the physiological values described above. To model the nerve terminals and vesicles, virtual volumes ( $V'_{nt}$  and  $V'_{ves}$ ) were used that are larger than the anatomic volumes of these regions. Enlarged virtual volumes were used to account for the concentration of mHED in the nerve terminals and vesicles due to asymmetrical uptake transport mechanisms. Although not necessarily anatomically or physiologically correct, for mathematical simplicity, it was assumed that  $V'_{nt} = V'_{ves}$ . We have not been able to find information on the anatomic volumes of either the cardiac nerve terminal or the vesicular volume that would allow us to constrain either of these values. Modeling analysis using ratios ranging from 0.4:1 to 1:4, did not demonstrate appreciable effect on the model solution; therefore, we assumed a 1:1 ratio. Finally, a relative dispersion of 0.55 was used to describe the distribution of flow in the multiple pathways of the model to account for flow heterogeneity (26,27). Flow heterogeneity is distinct from the relative dispersion, described above, of a tracer as it passes through a tube (coronary artery).

The vascular input function for all the tracers was obtained using deconvolution to fit the albumin dilution curve (28,29). The extracellular parameters [ $PS_g$ ,  $V_{isf}$  ( $= V_{isf1} + V_{isf2}$ ) and  $PS_{isf}$ ] were estimated by fitting the sucrose dilution curve using an automated nonlinear least squares optimizer routine (30).

To fit the mHED data, the values of  $PS_g$  and  $PS_{isf}$  determined for sucrose were multiplied by the ratio of the square roots of their molecular weights, 1.378, to correct for the difference in aqueous diffusion coefficients between sucrose and mHED (31). The value of  $V_{isf}$  determined for sucrose was used for the corresponding value of  $V_{isf}$  for mHED in the subsequent modeling of mHED kinetics. The mHED parameters ( $PS_{nt}$ ,  $V'_{nt}$ ,  $G_{seq}$  and  $PS_{ves}$ ) were estimated via optimization by simultaneously fitting the mHED outflow dilution curve and the tissue residue curve with the same model solution. The dilution curves and residue curves for mHED were given equal weighting in the optimization. The dilution curve  $h(t)$  data were weighted by the factor  $1/h(t)^{0.7}$  to improve the fitting of the tails. Without weighting, solutions did not consistently fit the tails of the curves because the tail data were four orders of magnitude below the peak of the curve. Therefore, the tail data contributed little to the overall sum of squares of the model fit, which was the objective function that was minimized by the optimizer routine. On the basis of sensitivity function analysis, it was determined that fitting the tails of the curves was important for increasing the accuracy of estimates of the parameters that are distant from the capillary, such as  $V'_{nt}$ ,  $G_{seq}$  and  $PS_{ves}$ . Optimization was repeated sequentially until the solutions converged. Because the indicator dilution curves were collected for only 90 sec, they mainly provided constraints on estimating  $PS_{nt}$ , while the residue curves that extended to 30 min provided adequate constraint for estimating  $G_{seq}$ ,  $V'_{nt}$  and  $PS_{ves}$ .

### Experimental Preparation: Dog

In a single dog that was undergoing PET studies as part of another study evaluating methods for quantitating myocardial oxygen consumption, we injected 7 mCi  $^{11}\text{C}$ -mHED with the anesthetized animal under basal conditions and again during a steady-state increase in myocardial work with a constant dobu-

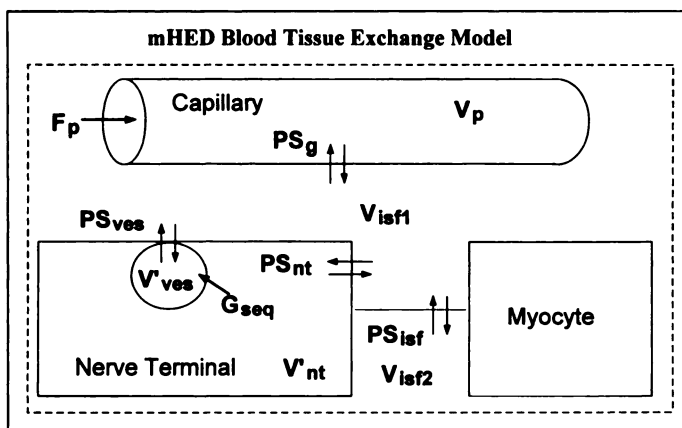


**FIGURE 1.** Conceptual model for a single capillary neuroeffector exchange unit for mHED.  $F_p$  = capillary flow (ml/min/g);  $PS_g$  = transport capacity through the endothelial clefts (ml/min/g);  $V_p$  = volume of capillary exchange unit (ml/g);  $V_{isf1}$  = volume of interstitial space close to the capillary membrane (ml/g);  $V_{isf2}$  = volume of interstitial space far from the capillary membrane, including space between the nerve terminal and the myocyte (neuroeffector junction) (ml/g);  $PS_{isf}$  = diffusional exchange between the interstitial space regions (ml/min/g);  $PS_{nt}$  = transport capacity across the nerve terminal membrane via the norepinephrine transporter mechanism (ml/min/g);  $V'_{nt}$  = virtual volume to account for storage of mHED within the nerve terminal but outside the vesicle (ml/g);  $V'_{ves}$  = virtual volume of vesicle, set equal to  $V'_{nt}$  for this study (ml/g);  $G_{seq}$  = sequestration of mHED within the vesicle (ml/min/g);  $PS_{ves}$  = transport capacity for release of mHED from the vesicles (ml/min/g).

tamine infusion that increased myocardial oxygen consumption by approximately 50%. PET images were acquired with a General Electric Advance PET scanner (GE Medical Systems, Waukesha, WI) with 18 detector rings and 35 image planes. For the mHED images, dynamic acquisition consisted of two 15-sec frames, nine 10-sec frames, six 30-sec frames and 11 300-sec frames. Images for determination of regional myocardial blood flow were acquired dynamically as follows beginning with a bolus injection of 7–10 mCi  $^{15}\text{O}$ -water: 15 2-sec frames and 25 10-sec frames. The images were reconstructed and reoriented into short-axis slices. Regions of interest (ROIs) were placed over the left atrium and midventricular tomographic slices, and decay-corrected time-activity curves were generated using a locally developed image display program: 4 view. The time-activity curves were read directly by the respective models for myocardial blood flow [Bergmann model (32,33)] and our mHED model (see below).

**Meta-Hydroxyephedrine PET Studies in a Dog.** An identical model was used for analyzing  $^{11}\text{C}$ -mHED time-activity curves from multiple ROIs in a dog heart. Additional a priori constraints were used in the analysis because no reference tracer data were available. In addition to the constraints described above for analyzing the rat heart data, it was assumed that  $PS_g = 0.75$  ml/min/g and that  $V_{isf} = 0.15$  ml/g, based on estimates of these parameters from multiple indicator dilution analysis of radiolabeled albumin and sucrose curves after intracoronary injection in the anesthetized dog (34). Coronary blood flow and a blood to tissue spillover coefficient, estimated by analyzing PET data from each ROI from a  $^{15}\text{O}$ -water study, were used in fitting the corresponding regional mHED curves. The vascular input function was the measured left atrial blood pool time-activity curve. The only parameters estimated via optimization of the mHED curves were  $PS_{nt}$ ,  $G_{seq}$ ,  $V'_{nt}$  and  $PS_{ves}$ . A sequence of five rounds of optimization was performed for each mHED curve, since it was found in preliminary trials that five rounds were sufficient to ensure convergence of the solutions.

## RESULTS

### Hemodynamics

For the rat heart, mean  $\pm$  s.d. values for heart rate, left ventricular systolic and diastolic blood pressures and coronary blood flow during the baseline and the DMI studies are shown in Table 1. There was a significant increase in heart rate, systolic blood pressure and coronary flow during the DMI perfusion.

### Modeling

An example of the indicator dilution curves (symbols) and the model solutions (lines) for the three radiotracers from one of the baseline studies is shown in the left panel of Figure 2. Passage of the radiotracers through the large vessels and arterioles and into the exchange vessels occurs during the initial 2–3 sec after injection, after which the curves begin to separate. The BSA curve had the highest peak, reflecting its rapid appearance in the outflow, because it remains in the intravascular space. Both sucrose and mHED had a slightly lower peak because they left the intravascular space and entered the interstitial space. Thus, less appears in the outflow samples. Soon after the peak, the sucrose curve crosses the other two, reflecting its rapid appearance in the outflow as it washes back from the interstitial space. There is no uptake of sucrose by the myocytes or trapping within the interstitial space. The amount of mHED appearing in the outflow remains lower than BSA throughout the period of collection, consistent with its being taken up in the nerve terminal or otherwise sequestered within the extravascular space. The right panel shows the simultaneous residue detection data for mHED for this same experiment. These MID/residue data were fit simultaneously with the model described above. Late in the outflow dilution fitting, the very slow clearance of mHED from the myocardium reflected in the residue curve becomes the driving force for the model solution, which causes the late tail of the MID model solution to be higher than the outflow data. Values for the seven model parameters describing the transport, volumes of distribution and retention of mHED that resulted in the lowest sum of squared errors of the model fit to the data are also shown.

Figure 3 shows the results during perfusion with 20 pM DMI. There was little effect on the very early portion of the curves; however, near the peak, both the sucrose and mHED curves were closer to the BSA curve, consistent with less of the compounds leaving the intravascular space (shorter transit time) and thus leaving more for early appearance in the outflow samples. After the peak of the curve, both sucrose and mHED appear in the outflow to a greater extent than does BSA. This is similar to the control situation for sucrose but reflects a major change in behavior for mHED. The mHED washes out of the interstitial space similar to sucrose and is consistent with NET blockade in the nerve terminal by DMI. The residue detection data provide additional evidence of NET blockade; the washout slope of the curve is much greater than during control conditions. Optimized values for the seven model parameters describing the transport, volumes of distribution and retention of mHED are also shown.

Table 2 shows the results for the calculated optimal parameter values for the experiments combining indicator dilution and residue detection data under control conditions and during DMI perfusion.  $PS_g$ ,  $V_{isf}$  and  $PS_{isf}$  were constant from experiment to experiment and were little affected by the addition of DMI to the perfusion medium.  $PS_{nt}$ ,  $V'_{nt}$  and  $G_{seq}$  were significantly reduced in the presence of DMI. The mean and the range of calculated parameter values for individual studies are shown in Figure 4.

**TABLE 1**  
Hemodynamic Values

	Heart rate (beats/m)	SBP (mmHg)	DBP (mmHg)	Coronary flow (ml/m/g)
Baseline (n = 5)	193 ± 42	103 ± 40	1.1 ± 1.6	9.3 ± 3.3
Desipramine (n = 3)	230 ± 57*	138 ± 32*	0.0 ± 0.0	11.2 ± 0.6*

\*p < 0.05 vs. baseline.  
SBP = systolic blood pressure; DBP = diastolic blood pressure.

We also tested (data not shown) model simplification by setting a value for  $G_{seq}$  equal to the average for all the control studies and then trying to fit the data optimizing on  $PS_{nt}$  and  $V'_{nt}$ . It was not possible to achieve a satisfactory fit adjusting only these two parameters.

To evaluate whether our model has potential clinical application, we tested it on a time series of PET mHED images from a dog studied at baseline and during dobutamine infusion, which increased the heart rate–systolic blood pressure product by ~twofold. Regions of interest were created on a midventricular short-axis image, and time-activity curves were generated. Examples of time-activity curves from images acquired at baseline and during dobutamine infusion are shown in Figures 5 and 6.

To model the PET data, the parameters  $PS_g$ ,  $V_{isf}$  and  $PS_{isf}$  for mHED were fixed to the values for these parameters for sucrose in the in vivo canine heart (34). This assumption was based on our observation that in the rat hearts  $PS_g$ ,  $V_{isf}$  and  $PS_{isf}$  were relatively constant among different hearts, were little affected by DMI and were similar to the values for sucrose. Thus, only four parameters were optimized to find the model solutions. The model fits and the optimized values for  $PS_{nt}$ ,  $V_{nt}$ ,  $G_{seq}$  and  $PS_{ves}$  for one ROI are shown in Figures 5 (baseline) and 6 (dobutamine). As can be appreciated, the fits are remarkably good and demonstrate a large difference between the normal state and dobutamine stimulation, suggesting that further evaluation of the model in in vivo settings is appropriate.

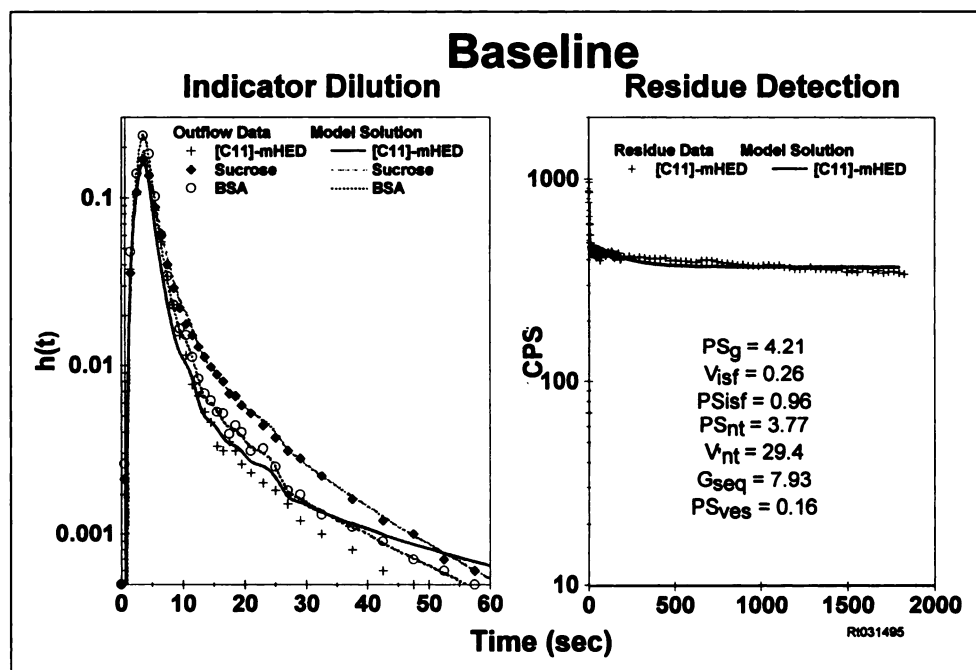
## DISCUSSION

These MID results provide the first description of the early time course of mHED transport and exchange between the vascular space, the interstitial space and the nerve terminal. The MID data (Fig. 2) show that mHED rapidly leaves the intravascular space. Presumably, the loss is through the interendothelial clefts, given the similarity of the mHED curves to those of sucrose. Blocking the neuronal NET mechanism with DMI (Fig. 3) had little effect on the early sucrose or mHED kinetics, which are dominated by the transport capacities of the interendothelial gap, the isf transport and the isf volume. None of these should be sensitive to NET blockade.

Neuronal function is described by the later part of the MID and residue curves. Under basal conditions, shown in Figure 2, sucrose rapidly washes out of the isf because there is no trapping mechanism and it is not metabolized. The mHED, on the other hand, remains below the albumin curve. This is consistent with rapid mHED uptake in the nerve terminals and very little subsequent release, as further substantiated by the flat slope of the mHED residue curve. Blocking NET function with DMI markedly changes the appearance of the mHED curves for both the MID and residue data (Fig. 3). During DMI perfusion, mHED appears in the outflow at a much greater rate than during the control period and approaches that of sucrose. That the two are not superimposable is consistent with incomplete blockade of the NET mechanism by the relatively low DMI concentration in the perfusate and the somewhat higher aqueous diffusion coefficient for mHED compared to sucrose. The greater decrease in the slope of the mHED residue curve is also consistent with more rapid clearance from the heart under the influence of DMI. When mHED is released from the nerve terminal back into the neuroeffector junction, it is washed out of the junction into the isf and, subsequently, the intravascular space so that a much smaller fraction undergoes the NET process.

Physiologic processes that govern the transport and storage capacities for mHED across membranes and interstitial spaces, and uptake and release from the nerve terminal, can be described in terms of permeability–surface area products and volumes of distribution. We have constructed an axially distributed blood–tissue exchange model that describes these pro-

**FIGURE 2.** Outflow dilution and residue detection data acquired simultaneously under basal conditions after bolus injection of  $^{125}$ I-bovine serum albumin,  $^3$ H-sucrose and  $^{11}$ C-mHED (symbols). The solid lines represent the mHED model fit simultaneously to the respective curves. The final values of each of the model parameters determined by optimization are also shown. (Left) Emphasis on the early data of the outflow dilution curves. (Right) Emphasis on the late data of residue detection.



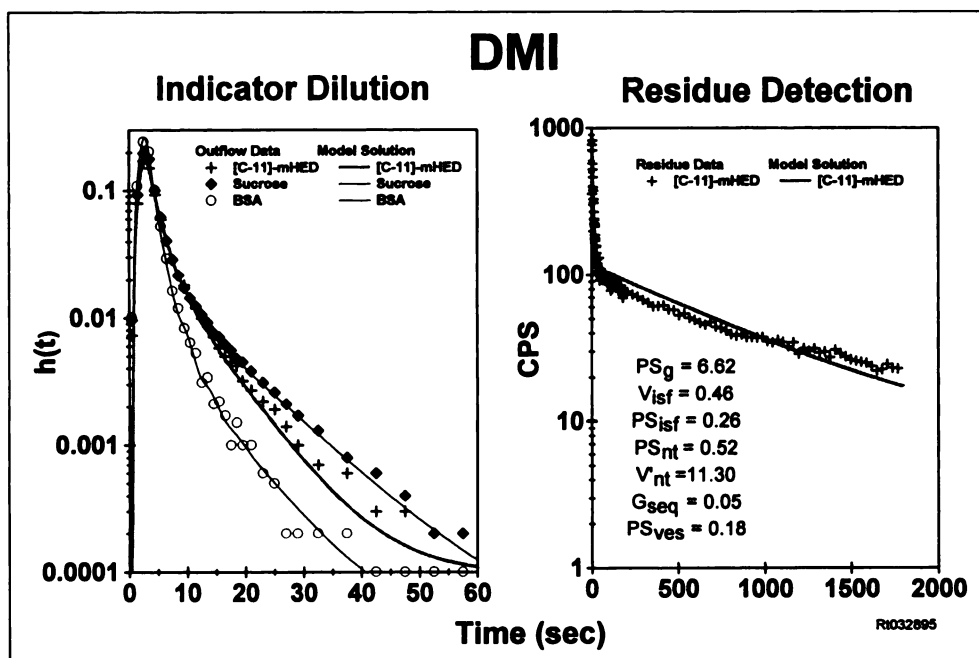


FIGURE 3. Simultaneously acquired outflow dilution and residue detection data during perfusion with 20 pM desipramine. Solid lines represent the mHED model fit simultaneously to the respective curves. The final values of each of the model parameters determined by optimization are also shown.

cesses. In this study, we have tested our model against the MID/residue detection data. Our results demonstrate that it is possible to quantitate the transport characteristics and the volumes of distribution for mHED using a model that approximates cardiac sympathetic nerve terminal structure and function. Furthermore, we have demonstrated that the model parameters change appropriately in response to perturbation. The model is limited, however, by lack of knowledge of certain anatomic volumes, e.g., neuronal and vesicular volumes and the structural constraints of representing vesicular exocytosis as a bidirectional process.

Although the parameters in our model are not directly comparable to those measures of mHED kinetics reported by DeGrado et al. (17), the basal uptake rate ( $K_1$ ) they reported for isolated perfused rat hearts of 2.7 ml/min/g is similar to the value for  $PS_{nt}$  that we observed, 4.8 ml/min/g.  $K_1$  from their study was directly measured from the rate of mHED uptake in the heart during a 10-min steady-state infusion. As such,  $K_1$  reflects the sum of the physiologic processes represented by our  $PS_g$ ,  $V_{isf}$ ,  $PS_{isf}$  and  $PS_{nt}$  but is dominated by the NET process and thus most closely corresponds to our  $PS_{nt}$ . DeGrado et al. (17) did not report a value for  $K_1$  after DMI, but, from the shape of the curves presented, it would have been markedly decreased, similar to the decrease in  $PS_{nt}$  that we observed.

Myocardial clearance of mHED from the normal heart is relatively slow. In the DeGrado et al. study (17), clearance, defined as  $k_2$ , was  $0.001 \text{ min}^{-1}$  and was assumed to be a monoexponential process. However, the authors pointed out

that several of the hearts had an early clearance that was significantly faster, but they did not include these data in the analysis. DMI increased their clearance rate. Our blood-tissue exchange model has no directly comparable measurement to their  $k_2$ , which lumps vesicular uptake/release and recycling of mHED at the NET site. In our model,  $k_2$  is reflected by the parameters  $PS_{nt}$ ,  $V'_{nt}$ ,  $G_{seq}$  and  $PS_{ves}$ , of which only  $PS_{nt}$  and  $G_{seq}$  were significantly sensitive to DMI blockade. However, excluding either  $V'_{isf}$  or  $PS_{ves}$  from the model prevented a satisfactory fit to the late portion of the residue curve during both the control period and DMI blockade. The absence of a change in  $PS_{ves}$  with DMI is consistent with its known minimal effect on vesicular function (35).

The volume of distribution,  $V'_{nt}$ , is a virtual volume; it does not have an anatomic equivalent because it reflects asymmetrical membrane transport into the nerve terminal. It would be much smaller than the  $V_d$  calculated by DeGrado as the ratio of the total heart mHED concentration to the perfusate concentration at equilibrium. The directional changes in the two should be similar; however, the effect of DMI on  $V_d$  was not determined in the DeGrado study.

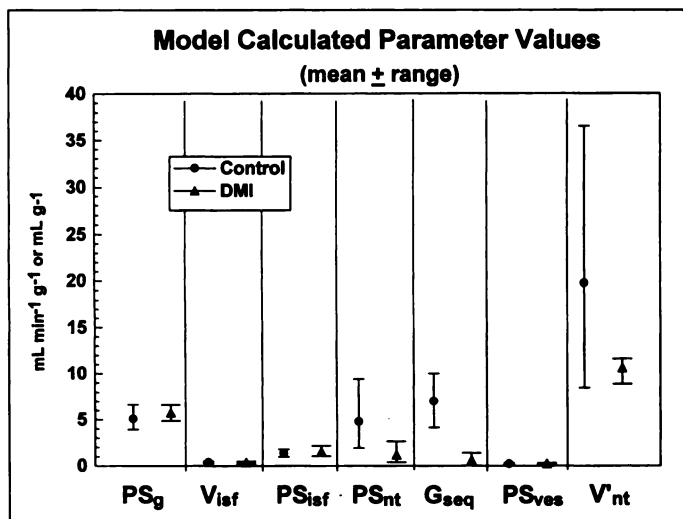
A potential source of error in our analysis of the rat data arises from our use of a value for capillary volume in the model of 0.035 ml/g. This is the value generally accepted for the canine model, but is less than that reported by Anversa et al. (36) (0.074 ml/g) for a different breed of rat than the one we used. If one uses the larger value in our model and repeats the optimization process, there is less than a 15% change in any of

TABLE 2  
Model Parameter Results

	$PS_g$ (ml/m/g)	$V_{isf}$ (ml/g)	$PS_{isf}$ (ml/m/g)	$PS_{nt}$ (ml/m/g)	$V'_{nt}$ (ml/g)	$G_{seq}$ (ml/m/g)	$PS_{ves}$ (ml/m/g)
Baseline (5 hearts)	$5.1 \pm 1.4$	$0.39 \pm 0.08$	$1.4 \pm 0.4$	$4.8 \pm 2.9$	$19.7 \pm 12.7$	$7.8 \pm 3.7$	$0.21 \pm 0.07$
Desipramine (3 hearts)	$5.8 \pm 0.9$	$0.36 \pm 0.13$	$1.5 \pm 0.6$	$1.2 \pm 1.3^*$	$10.6 \pm 1.5$	$0.60 \pm 0.68^*$	$0.23 \pm 0.06$

\* $p = 0.05$  vs. baseline.

$PS_g$  = transport capacity through the endothelial clefts (ml/m/g);  $V_{isf}$  = volume of interstitial space;  $PS_{isf}$  = diffusional exchange between the interstitial space regions (ml/m/g);  $PS_{nt}$  = transport capacity across the nerve terminal membrane via the reuptake 1 mechanism (ml/m/g);  $V'_{nt}$  = virtual volume to account for storage of mHED within the nerve terminal but outside the vesicle. (ml/g);  $G_{seq}$  = sequestration of mHED within the vesicle (ml/m/g);  $PS_{ves}$  = transport capacity for release of mHED from the vesicles (ml/m/g).



**FIGURE 4.** Model values determined by optimization for each of the parameters for the individual studies in the control state and during perfusion with desipramine. Abbreviations for parameter are the given in the legend to Figure 1.

the values for  $PS_g$ ,  $V_{isf}$ ,  $PS_{isf}$  or  $V'_{nt}$  during either control or DMI conditions. The values for  $PS_{nt}$ ,  $G_{seq}$  and  $PS_{ves}$  are somewhat larger, but they demonstrate the same directional changes with DMI and do not change our conclusions.

#### Potential Application to Image Analysis

Functional evaluation of the regional cardiac presynaptic SNS will be increasingly important as we try to understand the pathophysiology linking congestive heart failure and sudden cardiac death or depression and sudden death. Imaging neuro-receptors with radiolabeled sympathetic effectors or their analogs would seem to have a great potential role. However, because of the complexities of the system, e.g., norepinephrine recycling, vesicular storage and release and multiple metabolic pathways, interpreting the kinetics of radiolabeled norepinephrine or its precursors has proven difficult (12). A qualitative or semiquantitative approach to image analysis is likely to be inadequate for more than the most superficial understanding.

Hutchins et al. (20) developed a compartmental model that demonstrated a positive correlation between model-estimated

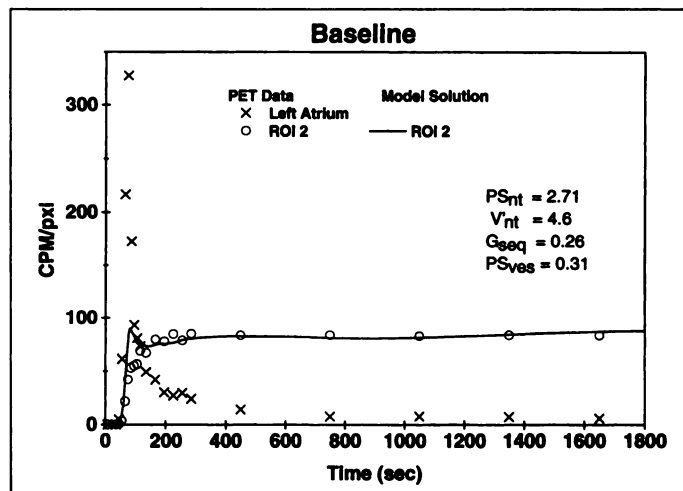


**FIGURE 5.** Left atrial and myocardial region of interest (ROI) time-activity curves (symbols) from PET images in a normal dog after intravenous injection of mHED. The solid lines represent the mHED model simultaneously fit to the respective curves. The final values of each of the model parameters determined by optimization are also shown. The very early peak in the model solution reflects spillover from the blood-pool activity.

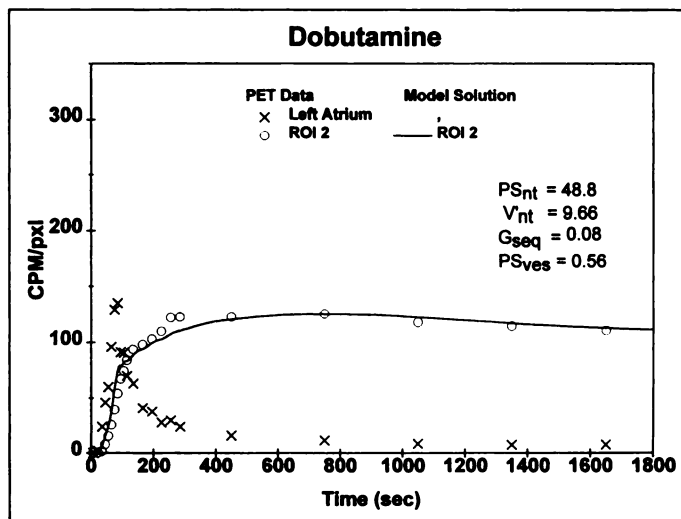


**FIGURE 6.** Left atrial and myocardial region of interest (ROI) time-activity curves (symbols) from PET images in a normal dog after intravenous injection of mHED. The heart rate-systolic blood pressure product had been increased twofold before the mHED injection and was maintained at this level during the period of image acquisition. Solid lines represent the mHED model simultaneously fit to the respective curves. The final values of each of the model parameters determined by optimization are also shown.

regional NE concentration and directly measured tissue concentration. However, this model reflected the anatomy-physiology of the presynaptic nerve terminal in only general terms and has not been applied to human studies. As described above, De-Grado et al. (17) have expanded understanding of mHED kinetics in the nerve terminal and proposed a more complete model, but have not evaluated it.

Our model accounts for the known barriers to uptake and release, volumes of distribution and sequestration capacities of the capillary-neuronal-effector unit and describes these in appropriate terms. The isolated heart studies demonstrate that presynaptic function can be quantitated from the kinetics of tracer-labeled mHED. There are, however, two major limitations to applying such a model to PET images. First, it is not possible to perform simultaneous multiple indicator dilution studies in humans or to even acquire images of multiple tracers simultaneously. It would be possible to perform sequential imaging of an intravascular marker, an interstitial marker and finally mHED. However, logistically and from a radiation dosimetry standpoint, this would not be practical. Second, the larger the number of parameters that must be solved in a model, the lower the probability that a unique single model solution would be found.

Our isolated heart studies demonstrate that these limitations can be overcome. Meta-hydroxyephedrine behaves similarly to sucrose in terms of transport into isf, and there is little or no effect of NET blockade on the initial transport or volumes of distribution. This is convincing evidence that these parameters can be fixed in the model, using known or separately measured values for sucrose. Fixing the value for sucrose would overcome the first limitation described above, and it would reduce the number of parameters to be fit to four, an acceptable number. The preliminary application of our model to PET images in a canine model (Figs. 5 and 6) suggests that such an approach is feasible. The model should be evaluated in a larger numbers of animals under a variety of conditions along with correlation of the model-estimated mHED concentration to direct tissue measurements of NE content to more completely validate this approach.

## CONCLUSION

We have developed an axially distributed blood-tissue exchange model for the NE analog mHED that accounts for the known transport capacities and volumes of distribution of the compound. In isolated perfused working rat hearts, we have demonstrated that the model solution closely fits the data from outflow dilution and residue detection experiments under control conditions and after blockade of the NET mechanism. The values for transport capacity and volumes of distribution calculated by the model are within the ranges reported by others using a different approach. Finally, we have shown that application of the model to PET images of mHED is feasible.

## ACKNOWLEDGMENTS

We acknowledge the technical assistance of John Cheng and James Ploger in data acquisition. This work was supported by the Department of Veterans Affairs Medical Research Service and National Heart Lung and Blood Institute Grants HL50238 and HL50239.

After a short illness, Dr. Kroll expired on July 15, 1997. This article is dedicated to his memory as a friend and collaborator.

## REFERENCES

1. Meredith IT, Broughton A, Jennings GL, Esler MD. Evidence of selective increase in cardiac sympathetic activity in patients with sustained ventricular arrhythmias. *N Engl J Med* 1991;325:618-624.
2. Francis GS, Cohn JN, Johnson G, Rector TS, Goldman S, Simon A. Plasma norepinephrine, plasma renin activity and congestive heart failure. *Circulation* 1993; 87:40-48.
3. Packer M. The neurohormonal hypothesis: a theory to explain the mechanism of disease progression in heart failure. *J Am Coll Cardiol* 1992;20:248-254.
4. Francis GS, McDonald NS, Cohn JN. Neurohumoral activation in preclinical heart failure: remodeling and the potential for intervention. *Circulation* 1993;87:IV90-IV96.
5. Veith RC, Lewis N, Linares OA, et al. Sympathetic nervous system activity in major depression: basal and desipramine-induced alterations in plasma norepinephrine kinetics. *Arch Gen Psychiatry* 1994;51:411-422.
6. Carney RK, Freedland KE, Rich M. Ventricular tachycardia and psychiatric depression in patients with coronary artery disease. *Am J Med* 1993;95:23-28.
7. Schwaiger M, Kalff V, Rosenspire K, et al. Noninvasive evaluation of sympathetic nervous system in human heart by positron emission tomography. *Circulation* 1990;82:457-464.
8. Schwaiger M, Hutchins GD, Kalff V, et al. Evidence for regional catecholamine uptake and storage sites in the transplanted human heart by positron emission tomography. *J Clin Invest* 1991;87:1681-1690.
9. Calkins H, Lehmann MH, Allman K, Wieland D, Schwaiger M. Scintigraphic pattern of regional cardiac sympathetic innervation in patients with familial long QT syndrome using positron emission tomography. *Circulation* 1993;87:1616-1621.
10. Merlet P, Delforge J, Syrota A, et al. Positron emission tomography with <sup>11</sup>C CGP-12177 to assess beta-adrenergic receptor concentration in idiopathic dilated cardiomyopathy. *Circulation* 1993;87:1169-1178.
11. Wieland DM, Hutchins GD, Rosenspire KC, et al. [<sup>11</sup>C]-Hydroxyephedrine (HED): a high specific activity alternative to 6-[<sup>18</sup>F]-fluorometaraminol (FMR) for heart neuronal imaging [Abstract]. *J Nucl Med* 1989;30:767.
12. Schwaiger M, Hutchins GD, Wieland DM. Noninvasive evaluation of the cardiac sympathetic nervous system with positron emission tomography. In: Bergmann SR,

- Sobel BE, eds. *Positron emission tomography of the heart*. Mount Kisco, NY: Futura Publishing, Inc., 1992:231-254.
13. Goldstein DS, Eisenhofer G, Dunn BB, et al. Positron emission tomographic imaging for cardiac sympathetic innervation using 6-[<sup>18</sup>F]-fluorodopamine: initial findings in humans. *J Am Coll Cardiol* 1993;22:1961-1971.
14. Nguyen NTB, DeGrado TR, Chakraborty P, Stafford K, Wieland D, Schwaiger M. Evaluation of C-11 epinephrine in isolated working rat heart [Abstract]. *J Nucl Med* 1993;34:45P.
15. Glowniak JV, Kilty JE, Amara SG, Hoffman BJ, Turner FE. Evaluation of metaiodobenzylguanidine uptake by the norepinephrine, dopamine and serotonin transporters. *J Nucl Med* 1993;34:1140-1146.
16. Raffel DM, Corbett JR, del Rosario RB, et al. Clinical evaluation of carbon-11-phenylephrine: MAO-sensitive marker of cardiac sympathetic neurons. *J Nucl Med* 1996;37:1923-1931.
17. DeGrado TR, Hutchins GD, Toorongian SA, Wieland DM, Schwaiger M. Myocardial kinetics of carbon-11-meta-hydroxyephedrine: retention mechanisms and effects of norepinephrine. *J Nucl Med* 1993;34:1287-1293.
18. Rosenspire KC, Haka MS, Van Dort ME, et al. A synthesis and preliminary evaluation of carbon-11-meta-hydroxyephedrine: a false transmitter agent for heart neuronal imaging. *J Nucl Med* 1990;31:1328-1334.
19. Link JM, Synovec RE, Krohn KA, Caldwell JH. High speed liquid chromatography of phenylethanolamines for the kinetic analysis of [<sup>11</sup>C]-meta-hydroxyephedrine and metabolites in plasma. *Chromatography B* 1997;693:31-41.
20. Hutchins GD, Schwaiger M, Haka MS, Rosenspire KC, Wieland DM. Compartmental analysis of the behavior of catecholamine analogs in myocardial tissue [Abstract]. *J Nucl Med* 1989;30:735.
21. Caldwell JH, Revenagh JR, Martin GV, et al. Comparison of <sup>18</sup>F-2-deoxy-D-glucose (FDG) and <sup>3</sup>H-fluoromisonidazole (FMISO) uptake during low-flow ischemia. *J Nucl Med* 1995;36:1633-1638.
22. Bassingthwaite JB, Goresky CA. Modeling in the analysis of solute and water exchange in the microvasculature. In: Renkin EM, Michel CC, eds. *Handbook of physiology: the cardiovascular system*. New York: American Physiology Society; 1984:549-626.
23. Kuikka J, Levin M, Bassingthwaite JB. Multiple tracer dilution estimates of D- and 2-deoxy-D-glucose uptake by the heart. *Am J Physiol* 1986;250:H29-H42.
24. King RB, Deussen A, Raymond GR, Bassingthwaite JB. A vascular transport operator. *Am J Physiol* 1993;265:H2196-H2208.
25. Bassingthwaite JB, Yipintsoi T, Harvey RB. Microvasculature of the dog left ventricular myocardium. *Microvasc Res* 1974;7:229-249.
26. Bassingthwaite JB, King RB, Rogers SA. Fractal nature of regional myocardial blood flow heterogeneity. *Circ Res* 1989;65:578-590.
27. King RB, Bassingthwaite JB, Hales JRS, Rowell LB. Stability of heterogeneity of myocardial blood flow in normal awake baboons. *Circ Res* 1985;57:285-295.
28. Bassingthwaite JB. Physiology and theory of tracer washout techniques for the estimation of myocardial blood flow: flow estimation from tracer washout. *Prog Cardiovasc Dis* 1977;20:165-189.
29. Bassingthwaite JB. Circulatory transport and the convolution integral. *Mayo Clin Proc* 1967;42:137-154.
30. Nelder JA, Mead R. SIMPLEX. *Comput J* 1965;7:308-311.
31. Stein WD. *Transport and diffusion across cell membranes*. Orlando: Academic Press; 1986.
32. Bergmann SR, Herrero P, Markham J, Weinheiner CJ, Walsh MN. Noninvasive quantitation of myocardial blood flow in human subjects with oxygen-15-labeled water and positron emission tomography. *J Am Coll Cardiol* 1989;14:639-652.
33. Herrero P, Markham J, Bergmann SR. Quantitation of myocardial blood flow with H<sub>2</sub>[<sup>15</sup>O] and positron emission tomography: assessment and error analysis of a mathematical approach. *J Comput Assist Tomogr* 1989;13:862-873.
34. Kroll K, Stepp DW. Adenosine kinetics in the canine coronary circulation. *Am J Physiol* 1996;270:H1469-H1483.
35. Iversen LL. Uptake processes for biogenic amines. In: Iversen LL, Iversen SD, Snyder SH, eds. *Handbook of psychopharmacology*. New York: Plenum Press; 1975:381-442.
36. Anversa P, Olivetti G, Melissari M, Loud AV. Stereological measurement of cellular and subcellular hypertrophy and hyperplasia in the papillary muscle of adult rat. *J Mol Cell Cardiol* 1980;12:781-795.